An Inverse Problem Approach to the Correction of Distortion in EPI Images

Patrice Munger, Gerard R. Crelier, Terry M. Peters, *Senior Member, IEEE*, and G. Bruce Pike*, *Member, IEEE*

Abstract—Magnetic resonance imaging using the echo planar imaging (EPI) technique is particularly sensitive to main (B_0) field inhomogeneities. The primary effect is geometrical distortion in the phase encoding direction. In this paper, we present a method based on the conjugate gradient algorithm to correct for this geometrical distortion, by solving the EPI imaging equation. Two versions are presented: one that attempts to solve the full four-dimensional (4-D) imaging equation, and one that independently solves for each profile along the blip encoding direction. Results are presented for both phantom and *in vivo* brain EPI images and compared with other proposed correction methods.

Index Terms—Conjugate gradient method, distortion, echo-planar imaging (EPI), image processing, magnetic resonance imaging (MRI), reconstruction.

I. INTRODUCTION

AN IMPORTANT source of degradation of echo planar images (EPI) is the phase error introduced by the main (B_0) field inhomogeneity along the EPI trajectory. Although this phase error is predictable for a point-object (it increases linearly along the trajectory), it is nonlinear when the signal comes from different points of the object with different local B_0-values (Fig. 1). The most adverse effect of these phase errors is geometrical distortion. These distortions can be troublesome in various applications, including surgical guidance and correlation of functional magnetic resonance imaging (fMRI) data with anatomical information from different sources.

Several methods have been suggested to address the distortion problem in EPI images. Some of these correct distortion directly in image space using a B_0-field map [1] or two acquisitions having different polarity of the phase encoding gradient [2]. Other methods apply a phase correction to the k-space data before performing normal two-dimensional (2-D) fast Fourier transform (FFT) reconstruction [3], [4]. All of these methods approach the EPI distortion problem on a column-by-column basis, by independent one-dimensional (1-D) corrections of the EPI image along the phase encoding direction. This 1-D processing approach is based on the assumption, which is valid in a wide range of conditions, that the EPI point spread function (PSF) is 1-D.

P. Munger, G. R. Crelier and *G. B. Pike are with the Magnetic Resonance Imaging, Montreal Neurological Institute, Montreal, PQ, H3A 2B4, Canada (e-mail: bruce@bic.mni.mcgill.ca).

T. M. Peters is with the John P. Robarts Research Institute, University of Western Ontario, ON, N6A 5C1, Canada.

The approach proposed in this paper consists of using the theoretical relationship between the distorted EPI image obtained from 2-D FFT reconstruction and the "true" undistorted image to set up a system of linear equations that can be solved [5]. This method can be applied either on a column-by-column basis, as proposed in [6], or in a full 2-D solution. Furthermore, the generality of the inverse problem approach allows us to apply it to non-EPI restoration problems as well, as shown by Man *et al.* for projection reconstructed MR data [7].

II. THEORY

A. EPI Image Formation

The single-shot EPI sequence [8] acquires the entire k-space data matrix in one excitation. In the blipped EPI method [9], an oscillating readout gradient is applied, together with the short blipped phase encoding gradient [Fig. 2(a)]. If data are sampled only during the constant portion of the readout gradient, the resulting k-space sampling is uniform. When data are acquired during the ramp-up or ramp-down period of the readout gradient, the k-space data resulting from a uniform temporal sampling rate are nonuniform. In order to obtain uniformly spaced points in k-space, one can use a nonuniform sampling rate [10] or perform interpolation [11] of the nonuniform data before reconstruction by inverse FFT. The EPI sequence discussed in this paper uses the first method (nonuniform sampling rate) so that no interpolation is required. The k-space trajectory is as shown in Fig. 2(b).

B. EPI Imaging Equation

In the presence of B_0-field inhomogeneity, the discrete data collected during a 2-D MRI acquisition can be expressed as a linear transformation between the ideal $M \times N$ image $I_{m,n}$ and the measured signal $S_{k,l}$ [12]

$$S_{k,l} = \sum_{m=0}^{M-1} \sum_{n=0}^{N-1} I_{m,n} A_{m,n;k,l} \tag{1}$$

with

$$A_{m,n;k,l} = e^{-2\pi i((km/M)+(ln/N)+(\gamma/2\pi)\Delta B_{m,n}t_{k,l})} \tag{2}$$

where

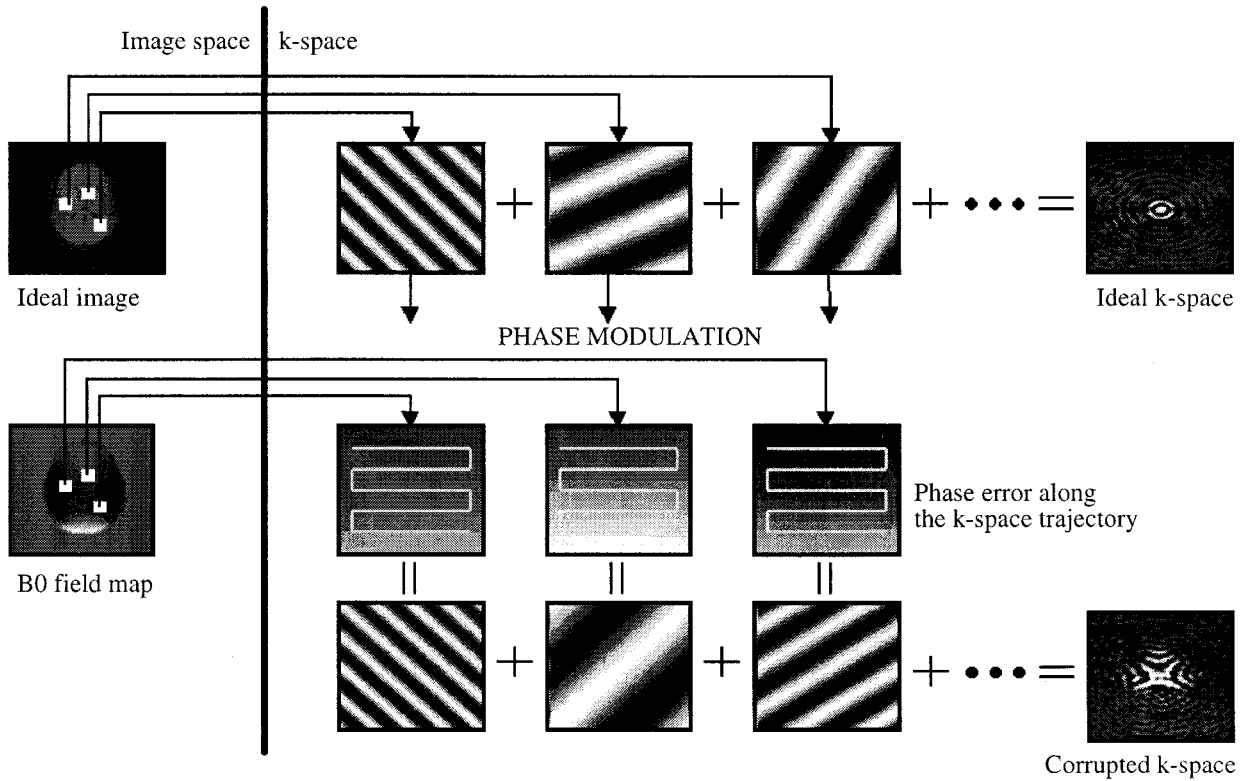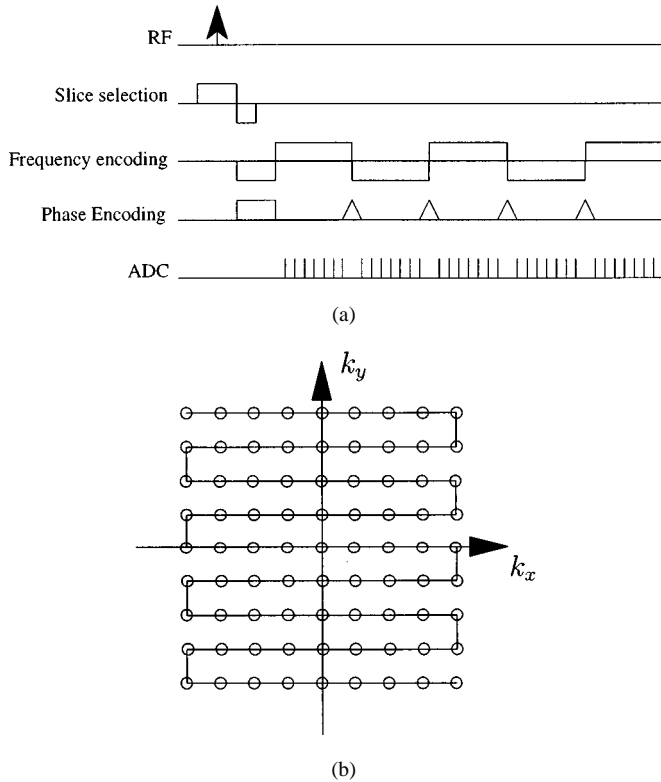|	
m and n	vertical and horizontal spatial variables;
M and N	vertical and horizontal image matrix size;
$\Delta B_{m,n}$	spatially variant B_0-field inhomogeneity;
$t_{k,l}$	time between the sampling of the k-space point (k, l) and the RF excitation.

Fig. 1.   The EPI image process.

Fig. 2.   (a) Blipped EPI sequence and (b) K-space trajectory.

This last parameter depends on the k-space trajectory that we assume to be perfect (i.e, the gradient timing and spatial linearity are assumed to be ideal).

Equation (1) can be transformed into a relation between the FT reconstructed image $I'_{m',n'}$ and the ideal image $I_{m,n}$ by taking the 2-D FFT of $A_{m,n;k,l}$ with respect to k and l on both sides of (1) for each value of m and n. Mathematically

$$I'_{m',n'} = \sum_{m=0}^{M-1} \sum_{n=0}^{N-1} I_{m,n} K_{m,n;m',n'} \tag{3}$$

where $K_{m,n;m',n'} = $ 2-D IFFT $(A_{m,n;k,l})$; i.e.,

$$K_{m,n;m',n'}$$

$$= \sum_{k=0}^{M-1} \sum_{l=0}^{N-1} A_{m,n;k,l} e^{2\pi i((km'/M)+(ln'/N))} \tag{4}$$

$$= \sum_{k=0}^{M-1} \sum_{l=0}^{N-1} e^{2\pi i((k(m'-m)/M)+(l(n'-n)/N)-(\gamma/2\pi)\Delta B_{m,n} t_{k,l})}. \tag{5}$$

We note that $K_{m,n;m',n'}$ is the 2-D PSF associated with voxel (m,n). Depending on the particular form of the PSF, some simplifications to this equation may be possible. Using integral equation terminology, we refer to $K_{m,n;m',n'}$ as the *kernel* of the EPI imaging equation.

The main rationale for expressing the equation in the form (3) is that the kernel of this equation has a sparse structure, as opposed to the kernel of (1). We will show how this four-dimensional (4-D) equation can be solved directly using sparse matrices and the conjugate gradient method, leading to a general 2-D correction approach. Also, the particular form of the EPI kernel will lead to an important simplification of this equation, allowing the 2-D problem to be decomposed into a series of 1-D problems.
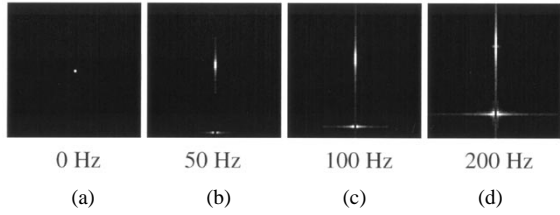
Fig. 3. EPI PSF corresponding to B_0-fields offsets of (a) 0 Hz, (b) 50 Hz, (c) 100 Hz, and (d) 200 Hz. The EPI parameters are matrix size $= 128 \times 128$, TE $= 65$ ms, and $T_{\text{acq}} = 123$ ms.

C. EPI Point Spread Function (PSF)

It is interesting to look at the effect on a point-object of the phase errors in the EPI imaging process. Consider a point-object $I_{m,n} = \delta_{m,0}\delta_{n,0}$. From (3)

$$\text{PSF}_{m',n'} = \sum_{m=0}^{M-1}\sum_{n=0}^{N-1}\delta_{m,0}\delta_{n,0}K_{m,n;m',n'} \qquad (6)$$

$$= K_{0,0,m',n'} \qquad (7)$$

$$= \sum_{k=0}^{M-1}\sum_{l=0}^{N-1}e^{2\pi i((km'/M)+(ln'/N)-(\gamma/2\pi)\Delta B_{0,0}t_{k,l})}. \qquad (8)$$

Fig. 3 illustrates the EPI PSF for several different frequency offset values. Note that the PSF extends in both dimensions and four distinct effects can be observed, as follows

- geometrical distortion, a consequence of the shift of the main peak in the phase encoding direction, which is proportional to the frequency offset;
- blurring in the phase encoding direction, demonstrated by the spread of the main peak;
- ghosting in the phase encoding direction, indicated by the presence of secondary peaks, which is especially important for larger frequency offsets;
- blurring of the ghosts, mainly in the frequency encoding direction.

We note that ghosting in EPI may have other causes that can be more important than the shape of the PSF. One of these factors is the misalignment of the analog-to-digital conversion (ADC) window with the time-varying gradients [13]. A misalignment of even a fraction of the intersample spacing can cause significant ghosting in the image.

Although the PSF is 2-D, it can be approximated by a one-dimensional function for small field offsets. This fact will be exploited to justify 1-D processing.

D. Matrix Formulation

The 4-D tensor equation (3) can be reformulated in terms of a matrix equation for both the case of 2-D and 1-D reconstructions.

1) 2-D Correction: If $\tilde{\mathbf{I}}'$ and $\tilde{\mathbf{I}}$ are the $MN \times 1$ vectors formed by rescanning $I'_{m',n'}$ and $I_{m,n}$ columnwise, i.e,

$$\tilde{I}_{m+Mn} = I_{mn} \qquad (9)$$

$$\tilde{I}'_{m'+Mn'} = I'_{m'n'} \qquad (10)$$

and $\tilde{\mathbf{K}}$ is the $MN \times MN$ matrix defined by

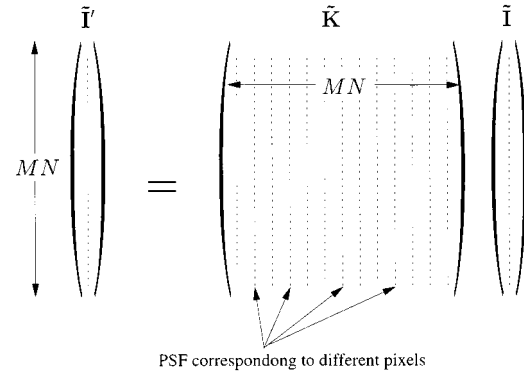$$\tilde{K}_{m'+Mn',m+Mn} = K_{m,n;m',n'} \qquad (11)$$

Fig. 4. Four-dimensional tensor equation in matrix form.

(3) takes the form of the $MN \times MN$ linear system

$$\tilde{\mathbf{I}}' = \tilde{\mathbf{K}}\tilde{\mathbf{I}}. \qquad (12)$$

This is illustrated in Fig. 4.

In the absence of field inhomogeneity, the matrix $\tilde{\mathbf{K}}$ is the identity matrix. It is easy to see that with a small amount of inhomogeneity, $\tilde{\mathbf{K}}$ will be close to the identity matrix and consequently sparse. This can be better appreciated by noting that the $(m+Mn)$th column of $\tilde{\mathbf{K}}$ is the column rescanning [14] of the 2-D EPI PSF corresponding to the pixel $I_{m,n}$, which contains only a few significant pixels when the field offset is small.

We also note that the geometrical distortion is reflected by a vertical shift of the diagonal elements of the $\tilde{\mathbf{K}}$ matrix (Fig. 5).

2) 1-D Correction: The particular form of the EPI PSF suggests that in the case in which field offsets are relatively small, 1-D processing can be performed on each column of an image. This approximation has many advantages. First, the solution of the large 4-D linear system is replaced by a set of smaller and more manageable 2-D linear systems.

The 4-D tensor equation (1) can be simplified by making the approximation that $t_{k,l}$ depends only on k. Equation (1) then becomes

$$S_{k,l} = \sum_{m=0}^{M-1}\sum_{n=0}^{N-1}I_{m,n}e^{-2\pi i((km/N)+(ln/N)+(\gamma/2\pi)\Delta B_{m,n}t_k)}. \qquad (13)$$

Performing an inverse FFT with respect to l, we obtain

$$S'_{k,n'} = \sum_{l=0}^{N-1}\sum_{m=0}^{M-1}\sum_{n=0}^{N-1}$$
$$\cdot I_{m,n}e^{-2\pi i((km/M)+(l(n-n')/N)+(\gamma/2\pi)\Delta B_{m,n}t_k)}$$
$$= \sum_{m=0}^{M-1}\sum_{n=0}^{N-1}I_{m,n}$$
$$\cdot e^{-2\pi i((km/N)+(\gamma/2\pi)\Delta B_{m,n}t_k)}\sum_{l=0}^{N-1}e^{-2\pi i((n-n')l/N)}$$
$$= \sum_{m=0}^{M-1}\sum_{n=0}^{N-1}I_{m,n}e^{-2\pi i((km/N)+(\gamma/2\pi)\Delta B_{m,n}t_k)}\delta_{n'n}$$
$$= \sum_{m=0}^{M-1}I_{m,n'}e^{-2\pi i((km/M)+(\gamma/2\pi)\Delta B_{m,n'}t_k)} \qquad (14)$$
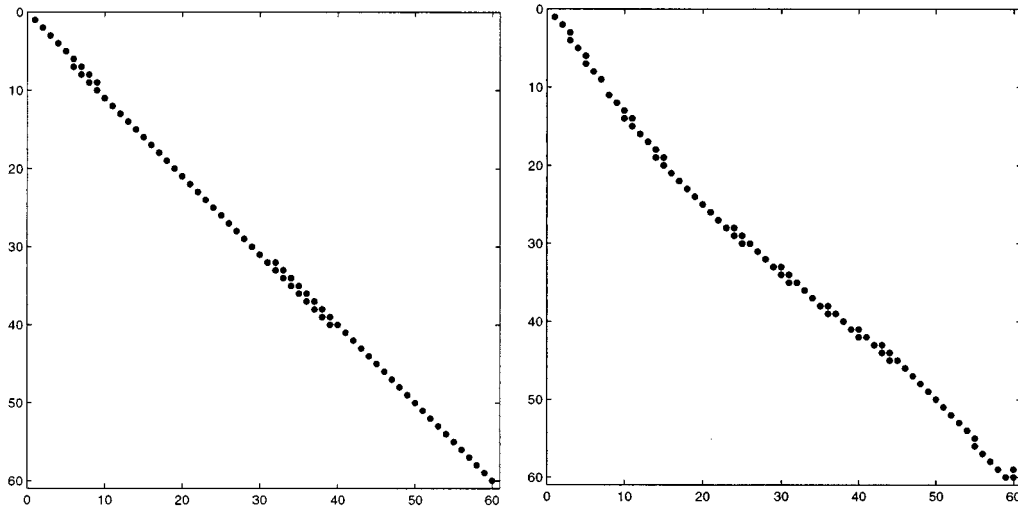
Fig. 5. Sparsity structure of a subregion of the kernel for small- (left) and large-field (right) inhomogeneity.

which can be expressed in matrix form as

$$\mathbf{S}_n = \mathbf{A}_n \mathbf{I}_n, \qquad n = 0 \cdots N - 1 \tag{15}$$

where $\mathbf{S}_m$ and $\mathbf{I}_m$ are the mth column of S'_{kn} and I_{mn}, respectively, and $\mathbf{A}_n$ is the $M \times M$ matrix defined by

$$[A_n]_{km} = e^{-2\pi i((km/M) + (\gamma/2\pi)\Delta B_{m,n} t_k)}. \tag{16}$$

This approximation effectively decouples the $MN \times MN$ linear system into N linear systems of size $M \times M$.

As in the 4-D case, (15) may be expressed in terms of the distorted image by performing a 1-D inverse FFT with respect to k on both sides of the equation, leading to

$$\mathbf{I}'_n = \mathbf{K}_n \mathbf{I}_n, \qquad n = 0 \cdots N - 1 \tag{17}$$

where $\mathbf{K}_n = \mathbf{F}^{\dagger} \mathbf{A}_n$, and $\mathbf{F}$ is the discrete Fourier transform matrix $F_{mn} = e^{-2\pi i(mn/M)}$. The $\dagger$ represents the Hermitian transposition (complex conjugation plus transposition).

III. METHODS

A. Conjugate Phase Reconstruction

The conjugate phase reconstruction method attempts to correct the EPI image by undoing the phase errors for each point of the image using the information provided by the B_0-field map. Using the formalism of the previous section, this is equivalent in 2-D to

$$\tilde{\mathbf{I}}^{cp} = \tilde{\mathbf{K}}^{\dagger} \tilde{\mathbf{I}}' \tag{18}$$

and in 1-D to

$$\mathbf{I}_n^{cp} = \mathbf{K}_n^{\dagger} \mathbf{I}_n \qquad n = 0 \cdots N - 1. \tag{19}$$

B. Weisskoff Method

This method [3] creates synthetic k-space data from the distorted image as follows:

$$\mathbf{S}_n^w = \mathbf{A}_n^w \mathbf{I}'_n \tag{20}$$

with

$$[A_n^w]_{km} = e^{-2\pi i((km/M) - (\gamma/2\pi)\Delta B_{m,n} t_{k,n})} \tag{21}$$

which is Fourier transformed to form the corrected image $\mathbf{I}^w$,

$$\mathbf{I}_n^w = \mathbf{F}^{\dagger} \mathbf{A}_n^w \mathbf{I}'_n \qquad n = 0 \cdots N - 1. \tag{22}$$

Although this method may seem similar to the conjugate phase method, they differ as shown by writing (19) as

$$\mathbf{I}_n^{cp} = \mathbf{A}_n^{\dagger} \mathbf{F} \mathbf{I}_n \qquad n = 0 \cdots N - 1. \tag{23}$$

The difference appears in the fact that the conjugate phase method associates the undistorted B_0-map to the undistorted image, whereas Weisskoff's method associates the undistorted B_0-map to the distorted EPI image.

C. Conjugate Gradient Method

The conjugate gradient (CG) method is an iterative technique based on finding the minimum of the quadratic form

$$f(\mathbf{x}) = \mathbf{x}^{\dagger} \mathbf{K} \mathbf{x} + \mathbf{b}^{\dagger} \mathbf{x} + \mathbf{c} \tag{24}$$

where $\mathbf{b}$ and $\mathbf{c}$ are arbitrary vectors [15]. When the matrix $\mathbf{K}$ is symmetric and positive-definite, the quadratic form is a multidimensional parabola with a minimum at $\mathbf{x}_{\min} = \mathbf{K}^{-1}\mathbf{b}$. Thus, minimizing $f(\mathbf{x})$ is equivalent to solving the linear system $\mathbf{K}\mathbf{x} = \mathbf{b}$.

The main strength of the CG method is its efficiency in dealing with large sparse systems of linear equations. This is because the matrix $\mathbf{K}$ is only used through its multiplication with vectors, and this is a fast operation for sparse matrices. This is a particularly important consideration for solving the 4-D tensor form of the imaging equation. In the case in which $M = N = 64$, the matrix $\mathbf{K}$ has 4096×4096 elements, which would require 256 Mb of memory to allow such a matrix to be stored in double precision. For $M = N = 128$, the storage requirement would be 16 times larger, or 4 Gb. Another concern is the fact that the inverse (or pseudoinverse) of $\mathbf{K}$ may not be sparse at all, even when $\mathbf{K}$ is sparse, and this rules out direct methods of solution.

When the linear system is not symmetric, a solution can still be found with the CG method by solving the associated *normal equations* [16]

$$\mathbf{K}^{\dagger} \mathbf{K} \mathbf{x} = \mathbf{K}^{\dagger} \mathbf{b}. \tag{25}$$
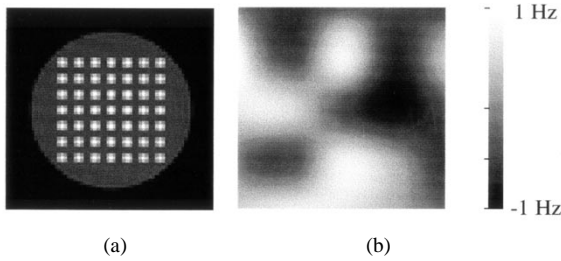
Fig. 6. (a) Analytic phantom and (b) B_0-field map used for simulations. This map was scaled in the simulations to provide various degrees of field inhomogeneity.

In the case in which the system is singular, CG can give a least-squares solution. Hestenes [17] derives a relation between the CG and the pseudoinverse of a matrix.

Attempting to solve the normal equations is not in general the best way to proceed because the condition number of the system equation ($\mathbf{K}^\dagger\mathbf{K}$) is the square of that of $\mathbf{K}$. However, other iterative methods for solving nonsymmetric systems of equations (e.g., the biconjugate gradient method) generally fail with complex systems. Although it is possible to express the normal equations in terms of real numbers (by splitting the real and imaginary parts), this involves a factor of 4 overhead in storage space and an additional factor of 2 penalty in computational effort [16]. This is hardly acceptable for such large linear systems of equation.

IV. RESULTS

We have performed simulations to evaluate the relative performance of the various distortion correction algorithm. We refer to these methods as CP1D (conjugate phase in 1-D), CP2D (conjugate phase in 2-D), CG1D (conjugate gradient in 1-D), CG2D (conjugate gradient in 2-D), and WEISS (Weisskoff method). The elements studied are the effect of the amplitude of the B_0-field offset, the effect of noise in EPI images, and the effect of noise in the B_0-map. For CG2D, the number of elements retained in the sparse kernel was $\approx 200\,000$, which corresponds to 1.2% of the total number of elements (64^4) in the full kernel. For CG1D and CP1D, the full 1-D kernel was used. For both CG1D and CG2D, the number of conjugate gradient iterations performed was three.

For these simulations, a 64×64 analytic phantom was created by sampling the exact Fourier components of an analytic object. A random, low spatial frequency field map was also created (Fig. 6) with a field offset range between -1 and 1 Hz. Scaling of this basic field map was used to provide different levels of field inhomogeneity.

Simulated EPI images were computed from the analytic phantom from (1) using a 64×64 k-space trajectory (TE = 35 ms, T_{acq} = 61 ms). The effective bandwidth in the phase encoding direction is ≈ 16 Hz ($1/T_{acq}$), which means that a B_0-field offset of 16 Hz would result in a spatial shift of one pixel in the phase encoding direction.

A. Effect of the Magnitude of the B_0-Field Inhomogeneity

EPI images were simulated with five different levels of field inhomogeneity: ± 16, ± 32, ± 48, ± 64, and ± 80 Hz. Recon-
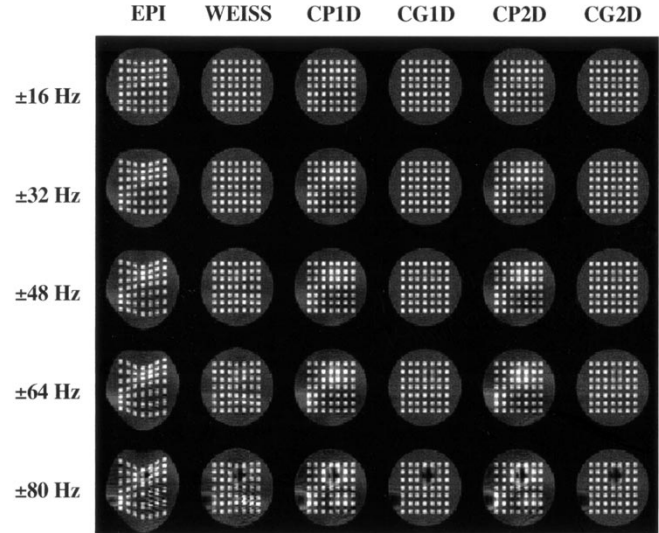

Fig. 7. Simulations on the effect of the amplitude of the B_0-field offset on the distortion correction.

TABLE I
RMS DIFFERENCES BETWEEN THE SIMULATED EPI FOR DIFFERENT AMPLITUDES OF B_0-FIELD OFFSET IN THE FIELD MAP, AND THE CORRECTED EPI FOR THE VARIOUS METHODS

B_0 off. amp. (Hz)	WEISS	CP1D	CG1D	CP2D	CG2D
$\pm$ 16.00	14.25	59.46	6.17	59.12	8.42
$\pm$ 32.00	47.52	118.57	13.59	118.80	12.91
$\pm$ 48.00	103.62	181.48	36.51	181.38	34.10
$\pm$ 64.00	180.06	247.15	65.32	247.31	61.87
$\pm$ 80.00	301.29	274.58	163.06	274.75	157.71

struction of these simulated EPI images was performed with the five methods. Results are shown in Fig. 7. Rms differences between the reconstructions and the analytic phantom are displayed in Table I.

Weisskoff's method works better than does conjugate phase reconstruction for small field offsets (16 and 32 Hz), mainly because of a better intensity inhomogeneity correction. However, geometrical distortion is not fully corrected for large field offsets (48–80 Hz).

Both the conjugate phase and CG methods correct geometrical distortions adequately. The main difference between the two is intensity variations that the conjugate phase methods do not correct.

The real benefit of the CG methods appears at larger B_0-field offsets (48–80 Hz), where both intensity inhomogeneity and geometrical distortions are corrected.

In both cases of conjugate phase and CG methods, no significant difference can be observed between the 1-D and the 2-D versions. This can be explained by the fact that the 1-D approximation of the EPI PSF is valid for all ranges of field offset used in the simulation.

At large field offsets (± 64 Hz), all methods fail to reconstruct adequately in regions where a large local B_0-field gradient is present. Nevertheless, the CG2D method provides a better reconstruction (based on rms deviation from the original) than do the other methods. Outside of these regions, the CG reconstruction again performs better than do the other methods. One
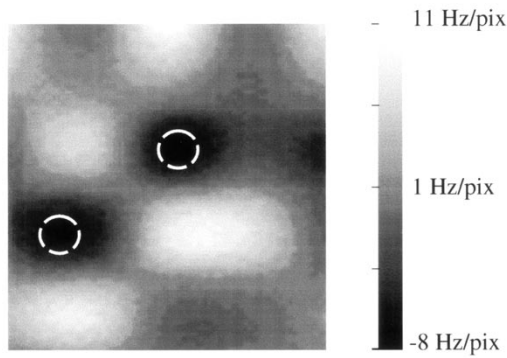
Fig. 8. Derivative of the ± 80-Hz B_0-map in the phase encoding direction. The white circles indicate regions with the largest negative B_0-inhomogeneity gradient in the phase encoding direction.
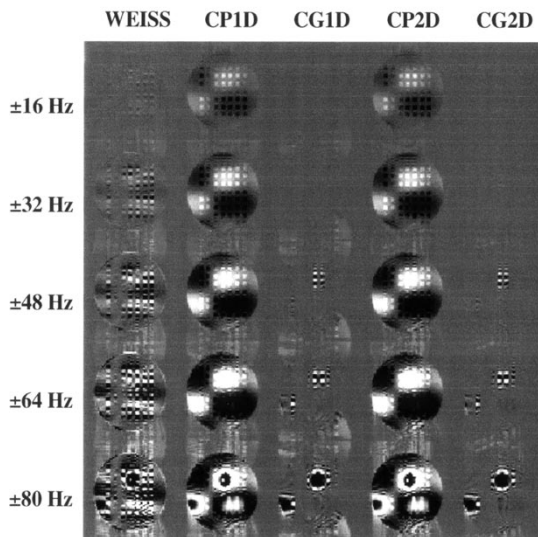

Fig. 9. Difference between the corrected images of Fig. 7 and the undistorted analysitc phantom image.

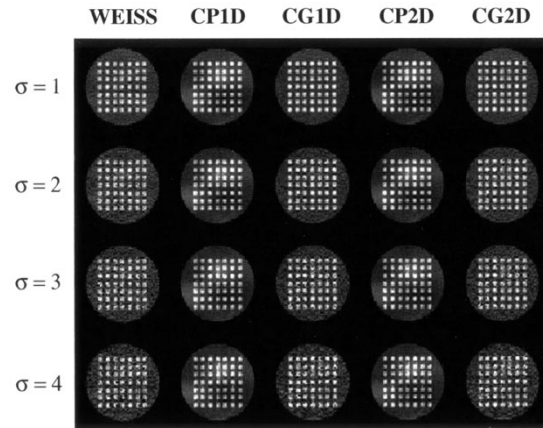| B_0 noise std (Hz)	WEISS	CP1D	CG1D	CP2D	CG2D
1.00	102.10	28.89	81.58	29.76	81.22
2.00	203.24	58.27	172.37	58.67	165.98
3.00	255.03	91.87	238.82	92.47	232.05
4.00	316.81	119.60	295.81	119.79	286.31

Fig. 10. Simulations on the effect of noise in of the B_0-map on the distortion correction.

The SNR was computed as the mean value of the corrected noiseless images, divided by the standard deviation of the image noise, estimated by the Rayleigh distribution corrected standard deviation of the background noise sampled in two rectangular regions on the side of each image

$$\text{SNR} = \frac{\text{mean(signal)}}{\text{std(signal)}} = \frac{\text{mean(signal)}}{\text{std(background)}} * \sqrt{2 - \pi/2}. \quad (26)$$

Results, shown in Table II, demonstrate little differences in the SNR obtained with the different methods.

C. Effect of Noise in B_0-Field Map

A simulated EPI image matrix was computed with a B_0-inhomogeneity range of ± 48 Hz. Reconstructions were then performed with different levels of Gaussian noise added to the field map (Fig. 10). The rms difference between the reconstructed images with the noisy B_0-map and the reconstructed images with the ideal B_0-map was computed and is shown in Table III.

D. Results on Real EPI Images

The correction methods were applied to real blipped EPI images of a phantom and of a volunteer's head (matrix size = 64×64, TE = 35 ms, T_{acq} = 61 ms) on a Siemens Vision 1.5-T scanner (Siemens Medical Systems, Erlangen, Germany). Nonuniform sampling of the signal was performed to obtain equally spaced points in k-space. This nonuniform sampling has been taken into consideration in the calculation of the kernel in (1). No phase correction was applied to the EPI raw data.

A normal spin echo sequence (matrix size = 64×64, TE1/TE2/TR = $10/14.48/400$ ms), interleaved with a second having the echo shifted by $\Delta t = 4.480$ ms, was used to

possible reason for the failure of the reconstruction in these regions of high local B_0-field gradient is that the kernel may become singular or badly ill-conditioned. This point can be better appreciated by looking at the B_0-field derivative in the phase encoding direction for the ± 80-Hz case (Fig. 8). The regions where reconstruction fails correspond exactly to the most negative B_0-derivatives. Note that negative derivatives are associated with compression in the distorted image, whereas positive derivatives are associated with stretching. It also appears that positive gradients, as opposed to negative gradients, do not affect the ability of CG to reconstruct perfectly.

The benefit of the 2-D processing over the 1-D processing may be better appreciated by looking at the difference images of Fig. 9. The CG2D method is the only one that can reduce significantly the B_0-inhomogeneity–induced ghosting artifacts.

B. Effect of Noise in EPI Images

In order to evaluate noise effects on the various correction methods, simulations were performed using the random field map with a frequency range of ± 48 Hz. All corrections methods were applied with the simulated EPI image on which different levels of complex white Gaussian noise was added.

TABLE III
RMS Differences Between the Image Reconstructed with Noisy B_0 Map and the Image
Reconstructed from Noiseless B_0-MAP

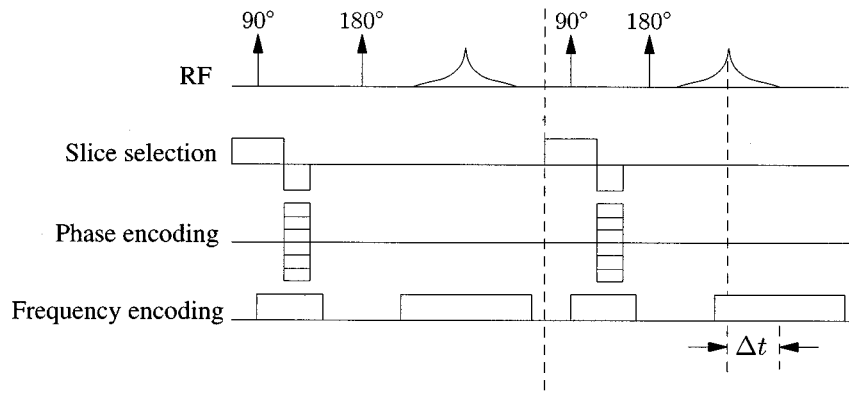| Simulated EPI	WEISS	CP1D	CG1D	CP2D	CG2D
28.89 ± 0.12	29.35 ± 0.13	29.67 ± 0.12	30.00 ± 0.13	29.67 ± 0.12	30.05 ± 0.12
19.72 ± 0.09	19.92 ± 0.09	20.24 ± 0.09	20.36 ± 0.09	20.25 ± 0.09	20.39 ± 0.09
9.97 ± 0.04	10.09 ± 0.04	10.33 ± 0.04	10.35 ± 0.04	10.33 ± 0.04	10.39 ± 0.04
5.00 ± 0.02	5.02 ± 0.02	5.16 ± 0.02	5.16 ± 0.02	5.17 ± 0.02	5.19 ± 0.02

Fig. 11. B_0-field mapping sequence.

generate the B_0-map (Fig. 11). The B_0-field map is obtained by subtracting the phases of the two acquisition. With this value of Δt, water and fat protons, although precessing at different rates, conserve the same relative phase at TE and TE$+\Delta$, which makes the phase difference observed between the two acquisitions dependent on static field inhomogeneity only and not on chemical shift [18]. We found that, for this example, phase unwrapping was not required. We note that, although the acquired field map is subject to distortion because of field inhomogeneity, the magnitude of these distortions is negligible compared with the distortions affecting the EPI image.

For the phantom acquisition, the field map was fitted with 2-D splines to remove noise. The B_0-map of the brain was filtered with a Gaussian kernel of full-width at half-maximum (FWHM) = 3 pixels.

The phantom reconstructions (Fig. 12) shows that the best distortion and intensity inhomogeneity correction are provided by CG1D and CG2D. The Weisskoff's method gives a good homogeneity correction, but the distortion correction is not complete. The CP1 and CP2 reconstructions correct for geometrical distortions but not for intensity inhomogeneity. As in the simulations, little difference can be noticed between the 1-D and the 2-D versions of CG and conjugate phase.

The *in vivo* experiment (Fig. 13) shows again the best performance of CG1D and CG2D. The intensity correction provided by the CG method can be seen on the difference image CG2D–CP1D. We also note that the Weisskoff method provides good distortion correction in low-distortion regions, but fails in high-distortion regions.

E. Computation Time

A important issue to be discussed is the computation time associated with the various reconstruction methods. All of
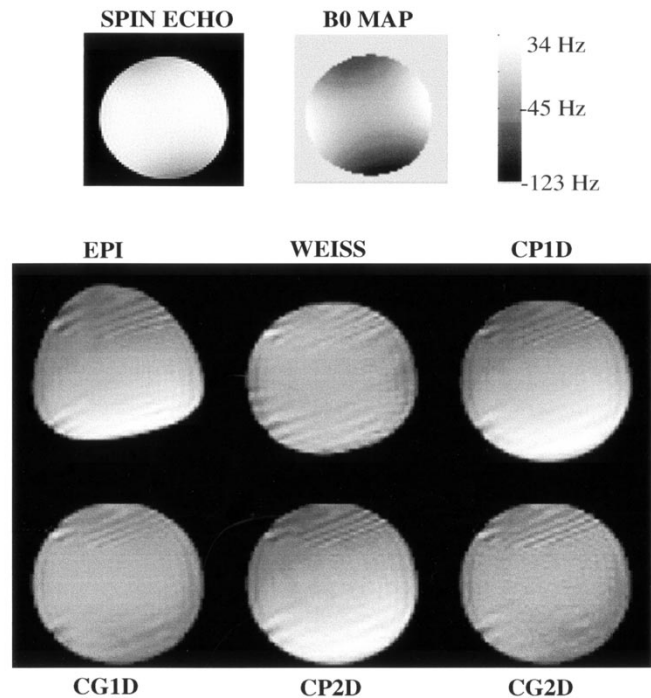

Fig. 12. Reconstruction with the various methods of the EPI image of a phantom.

the methods presented in this paper were implemented with MATLAB 5.0 (The MathWorks Inc., Natick, MA), on a Pentium 200-MHz running RedHat Linux 5.1. (RedHat, Durham, NC).

As an example, consider the *in vivo* brain experiment. The computation of the full 2-D kernel (used in CP2D and CG2D reconstructions) took around 2 min. Because it grows as N^4, it would take around 30 min for a 128×128 matrix size. Although
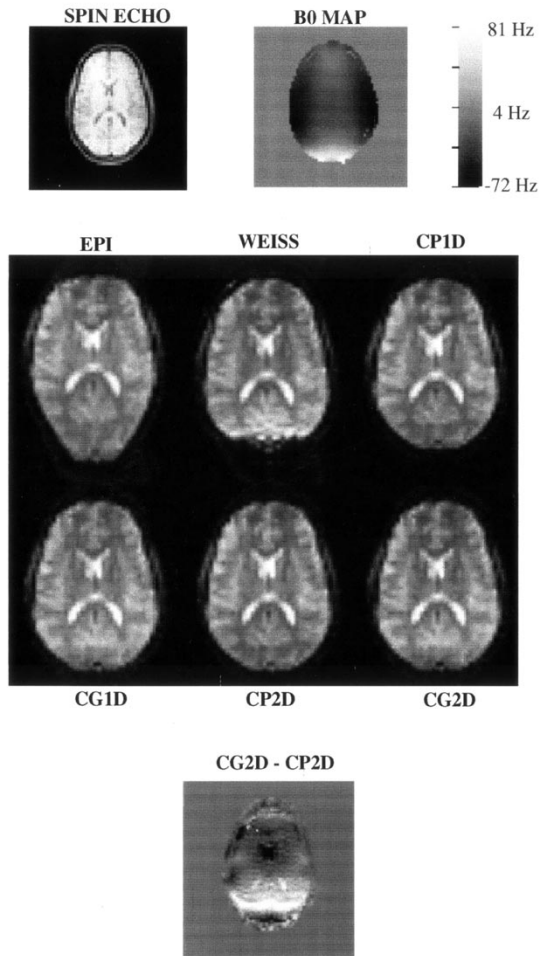
Fig. 13.   Distortion correction on a volunteer's head EPI image.

the calculation of the kernel may be expensive, it needs to be computed only once for a given B_0-map, which makes this time spent worthwhile for correcting a large number of images of the same slice (in dynamic functional MRI studies, for instance).

Once the kernel is computed, solving the system of equations with the CG method takes on the order of a few seconds per image. The time required is roughly proportional to the number of elements stored in the 2-D sparse kernel and the number of iterations performed. For the brain example, with the kernel having around 73 000 elements and two iterations, the computation time was 2 s.

One-dimensional kernel calculation is significantly faster than 2-D. The time required for the calculation of the 1-D kernel (used by CP1D and CG1D) was around 6 s. However, calculation of the solution was slightly longer than for the 2-D case. The two CG iterations took 3 s (recall that this involves the CG solution of 64, 64 $\times$ 64 systems of linear equations).

The Weisskoff reconstruction took 3.5 s. Note that it is also possible to implement this method as a two-step process: calculation of the kernel and computation of the corrected image. Therefore, the previous remark about the reconstruction of several images based on the same B_0-map also applies to this method.

V. CONCLUSION

This paper has presented a technique for correcting distortion in EPI images based on the CG method. It can be efficiently applied for the full resolution of the 4-D tensor imaging equation. However, when the field offsets are small, a simplification that allows 1-D processing on each column of the image may be used. This is because the phase variation occurs mainly in the blip encoding direction.

Our method was compared with previously proposed methods: the conjugate phase reconstruction and the Weisskoff method. We have shown that all methods work well for small field offsets, but the CG method leads to the best intensity homogeneity, even with a small number of iterations.

One particularly relevant application of this method is the correction of EPI functional MRI time series data, in which many hundreds of images of the same slices are acquired in a single session. Because the calculation of the kernel is decoupled from the computation of the solution of the equation system, it only has to be computed once. This allows a large number of dynamic images to be corrected in a reasonable amount of time.

It was shown that a 1-D processing is sufficient when field inhomogeneity is not too large. However, 2-D processing may be necessary when field offsets become large, such as in the case of fat signal, which has a field offset of approximately 200 Hz at 1.5 T.

Although the CG method does not significantly amplify the noise present in the EPI image, it is somewhat sensitive to noise in the field map. Thus, some preprocessing of the field map (e.g., low-pass filtering, polynomial or spline fitting) may be required. Because the field map is usually smooth, this preprocessing is not particularly problematic.

In practice, it was observed that the convergence of the CG method may be very fast in the case of EPI correction. In most cases, most of the correction was achieved after two iterations when the initial guess corresponded to the conjugate phase solution. In this case, the CG method can be thought of as a second-order correction over the conjugate phase solution.

The image restoration approach that we describe in this paper has already been applied for MRI projection data [7] and for 1-D correction of EPI images [6]. Application to other acquisition schemes may also be considered. However, the degree of correction and the rate of convergence may vary because of the different structure of the PSF. The effectiveness of the CG reconstruction on EPI data is because of the relatively simple form of the PSF.

REFERENCES

[1] P. J. Reber, E. C. Wong, R. B. Buxton, and L. R. Frank, "Correction of off resonance-related distortion in echo-planar imaging using epi-based field maps," *Magnetic Resonance Med.*, vol. 39, no. 2, pp. 328–330, Feb. 1998.

[2] R. Bowtell, D. J. O. McIntyre, M.-J. Commandre, P. M. Glover, and P. Mansfield, "Correction of geometric distortion in echo planar images," in *Proc. 12th Annu. Meeting SMRM*, 1993, p. 411.

[3] R. M. Weisskoff and T. L. Davis, "Correcting gross distortion on echo planar images," in *Proc. 11th Annu. Meeting SMRM*, 1992, p. 4515.

[4] K. Sekihara and H. Kohno, "Image restoration from nonuniform static field influence in modified echo-planar imaging," *Med. Phys. (USA)*, vol. 14, Nov.–Dec. 1987.

[5] E. M. Haacke, "Solving for nonideal conditions in two-dimensiodal Fourier transform magnetic resonance imaging using a generalized inverse transform," *Inv. Prob.*, vol. 3, no. 3, pp. 421–435, Aug. 1987.

[6] Y. M. Kadah and X. Hu, "Algebraic reconstruction for magnetic-resonance imaging under B_0 inhomogeneity," *IEEE Trans. Med. Imag.*, vol. 17, pp. 362–370, 1998.

[7] L. Man, J. M. Pauly, and A. Macovski, "Correcting severe local inhomogeneity blurs by spatially variant deconvolution," in *Proc. 12th Annu. Meeting SMRM*, 1993, p. 738.

[8] P. Mansfield, "Multi-planar image formation using nmr spin echoes," *J. Phys. C (GB)*, vol. 10, pp. L55–L58, Feb. 1977.

[9] I. L. Pykett and R. R. Rzedzian, "Instant images of the body by magnetic resonance," *Magnetic Resonance Med.*, vol. 5, pp. 563–571, Dec. 1987.

[10] F. Farzaneh, J. Riederer, and J. Pelc, "Analysis of T2 limitations and off-resonance effects on spatial resolution and artifacts in echo-planar imaging," *Magnetic Resonance Med.*, vol. 14, pp. 123–139, Apr. 1990.

[11] H. Bruder, H. Fischer, H. E. Reinfelder, and R. Schmitt, "Image reconstruction for echo planar imaging with nonequidistant k-space sampling," *Magnetic Resonance Med.*, vol. 23, pp. 311–323, Feb. 1992.

[12] D. G. Nishimura, "Principles of magnetic resonance imaging," Lecture Notes, 1994.

[13] M. H. Buonocore and L. Gao, "Ghost artifact reduction for echo planar imaging using image phase coffection," *Magnetic Resonance Med.*, vol. 38, pp. 89–100, July 1997.

[14] W. K. Pratt, *Digital Image Processing*. New York: Wiley, 1978.

[15] G. H. Golub and C. F. Van Loan, *Matrix Computations*. Baltimore, MD: John Hopkins Univ. Press, 1996.

[16] S. A. Teukolsky and W. T. Vetterling, *Numerical Recipes in C*. New York: William H. Press, 1993.

[17] M. R. Hestenes, "Pseudoinverse and conjugate gradients," *Commun. ACM*, 1975.

[18] G. H. Glover and E. Schneider, "Three-point Dixon technique for true water/fat decomposition with b_0 inhomogeneity correction," *Magnetic Resonance Med.*, vol. 18, 1991.